

Generalized Interpolation Material Point Approach to High Melting Explosive with Cavities Under Shock

X. F. Pan, Aiguo Xu, Guangcai Zhang and Jianshi Zhu

Laboratory of Computational Physics,
Institute of Applied Physics and Computational Mathematics, P. O. Box 8009-26,
Beijing 100088, P.R.China

E-mail: Xu_Aiguo@iapcm.ac.cn

Abstract. Criterion for contacting is critically important for the Generalized Interpolation Material Point(GIMP) method. We present an improved criterion by adding a switching function. With the method dynamical response of high melting explosive(HMX) with cavities under shock is investigated. The physical model used in the present work is an elastic-to-plastic and thermal-dynamical model with Mie-Grüneisen equation of state. We mainly concern the influence of various parameters, including the impacting velocity v , cavity size R , etc, to the dynamical and thermodynamical behaviors of the material. For the colliding of two bodies with a cavity in each, a secondary impacting is observed. Correspondingly, the separation distance D of the two bodies has a maximum value D_{\max} in between the initial and second impacts. When the initial impacting velocity v is not large enough, the cavity collapses in a nearly symmetric fashion, the maximum separation distance D_{\max} increases with v . When the initial shock wave is strong enough to collapse the cavity asymmetrically along the shock direction, the variation of D_{\max} with v does not show monotonic behavior. Our numerical results show clear indication that the existence of cavities in explosive helps the creation of “hot spots”.

PACS numbers: 62.50.+p; 62.20.Fe; 81.40.Lm

Submitted to: *J. Phys. D: Appl. Phys.*

1. Introduction

Cavitation phenomena are ubiquitous in nature, ranging from solid, liquid to plasma. Cavity creation and collapse play a very important role in a large amount of industrial processes, like erosion of materials, ignition of explosive, comminution of kidney stones, etc [1–3]. The cavitation phenomena may occur in a mesoscopic scale, but generally have a profound influence on the response in the macroscopic scale. As for explosives, the cavity collapse may result in jetting phenomena and consequently lead to a much higher temperature increase of the “hot spots”. Therefore, it has a potential to start local reaction leading to partial decomposition or run to full detonation [2]. On the one hand, cavitation acts as a means of increasing the sensitivity of explosive for ignition, but on the other hand, it represents a potential safety problem for handling such materials. The interest in both considerations inspired an amount of theoretical, experimental and numerical work aiming to study the influence of cavities to the explosives [2, 4–14].

During the collapse procedure explosive material under consideration is highly distorted and the boundaries should be tracked, which proposes a very high requirement to the numerical methods. In the early studies, conventional Eulerian and/or Lagrangian schemes were used [5–9]. When conventional Lagrangian methods are used, the mesh distortion associated with large deformations reduces the accuracy and will probably terminate the computations; ultimately, a re-meshing treatment is required, which is not a straightforward task and generally inefficient. It is known that the conventional Eulerian code is not convenient to track the boundaries. To continue, several mixed methods have been proposed to combine the merits of the two methods and overcome their drawbacks. Among them, the Arbitrary Lagrange-Euler(ALE) method [15] is a typical one. Several researchers have used the ALE method to study the collapse of cavities in explosive materials [16]. The particle-in-cell (PIC) is a second typical mixed method [17]. It also contributed to the research work on inhomogeneous plastic-bonded-explosives [18]. Additionally, a number of “meshless methods” have also been developed. To overcome the difficulty due to the distortion of mesh, the meshless method uses a series of discretized lagrangian points to construct the shape function. Some meshless methods, such as the Smooth Particle Hydrodynamics(SPH) [19–21], Dual Particle Dynamics(DPD) [22], etc, have been applied in the research of cavity collapse in explosive materials [22–24]. It should be mentioned that the microscopic Molecular Dynamics(MD) has also brought some new understanding of the physics and chemistry involved [12–14]. Yet, even with the most powerful computers in nowadays, the MD simulation is still far from reaching the practical spatial and temporal scales of real experiments [25].

The physical models used in previous numerical studies are mainly fluidic ones. Such models ignore many important characteristics of solid, like plastic strain, hardening, and effects relevant to the deformation history. In this study we revisit the Material Point Method(MPM) [26], recently developed in the field of computational solid physics, by presenting a new contact criterion, and then use it to study the dynamical

response of high melting explosive (HMX) with cavities under shock.

The MPM is a descendant of the PIC extended to solid mechanics [27–31]. Compared with the above-mentioned methods, the MPM provides a robust and efficient treatment of large deformation issues and a convenient framework for modeling contact between large numbers of contacting bodies. In MPM, each body is discretized by a collection of Lagrangian material points carrying all information required to advance the solution; the Eulerian background computational mesh is used to solve the governing equations and the mesh solution is then used to update the information on material points. Specifically, at each time step, the MPM calculations consist of two parts: a Lagrangian part and a convective one. Firstly, the computational mesh deforms with the body, and is used to determine the strain increment and the stresses carried by the particles. Then, the new position of the computational mesh is chosen (particularly, it may be the previous one); and the velocity field is mapped from the material points to the mesh nodes. This method has been applied to handle engineering problems with large strain [32,33] and/or dynamical energy release rate [34], fracture in heterogeneous material [35], dynamics failure [36,37], hypervelocity impact [38], thin membranes [39], granular materials [18,40–42], etc. The Generalized Interpolation Material Point (GIMP) method uses a variational form and a Petrov-Galerkin discretization scheme to overcome the numerical noise of previous MPM [26].

We study not only the collapse of cavities but also the deformation and dynamical response of cavities before collapsing under shock. These are important for understanding better the ignition of explosive. The elastic-to-plastic and thermal-dynamics model with the Mie-Grüneisen equation of state consulting the Rankine-Hugoniot curve is used to simulate the mechanical and thermal behaviors of the material. The model used here is more suitable for simulating the dynamical response of the solid material under shock than previous ones.

This paper is organized as follows. In Sect. 2 we briefly describe the generalized interpolation material point method where the contact algorithm is improved. In Sect. 3 the new scheme is validated by several benchmark tests and then is used to study cavitated high melting explosive. Sect. 4 concludes the present paper.

2. APPROACH

2.1. The Generalized Interpolation Material Point method

For continuum bodies, the conservation equation for mass is

$$\frac{d\rho}{dt} + \rho \nabla \cdot \mathbf{v} = 0. \quad (1)$$

where ρ is the mass density, \mathbf{v} is the velocity,

In GIMP and MPM, the continuum bodies are discretized with N_p material particles. Each material particle carries the information of position, velocity, temperature, mass, density, Cauchy stress, strain tensor and all other internal state variables necessary for the constitutive model. Since the mass of each material particle

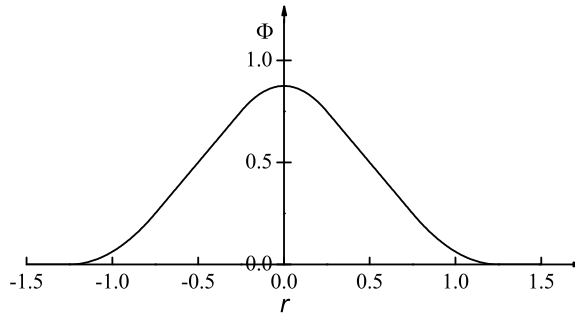


Figure 1. Contiguous particle GIMP weighting function in one dimension.

is equal and fixed, Eq.(1) is automatically satisfied. At each time step, the mass and velocities of the material particles are mapped onto the background computational mesh(grid). The mapped nodal velocity \mathbf{v}_j is obtained through the following equation,

$$\sum_j m_{ij} \mathbf{v}_j = \sum_p m_p \mathbf{v}_p N_i(\mathbf{x}_p) \quad (2)$$

where m_p , \mathbf{v}_p and \mathbf{x}_p are the mass, velocity and position of particle p , respectively. N_i is the shape function, i and j indexes of node.

In the early version of MPM, the grid shape function N_i is not smoothed in the construction of the weighting function which causes the numerical noise as the material points cross computational grid boundaries. Bardenhangen et al [26] presented a family of methods named the Generalized Interpolation Material Point(GIMP) methods in which the interpolation function are in C^1 (as opposed to MPM, for which are in C^0). In this paper the following smoothed shape function in C^1 is used, $N_i = \Phi(r_x)\Phi(r_y)$, where $r_x = |x_p - x_i|/L$, $r_y = |y_p - y_i|/L$, L is the length of cell, $\Phi(r)$ is given in flowing,

$$\Phi(r) = \begin{cases} \frac{7-16r^2}{16}, & r \leq 0.25 \\ 1 - r, & 0.25 < r \leq 0.75 \\ \frac{(5-4r)^2}{16}, & 0.75 < r \leq 1.25 \\ 0, & r > 1.25 \end{cases} \quad (3)$$

See also Fig.1. Eq.(3) is a weighting function with support in adjacent cells and the next nearest neighbor cells. This specialization has the advantage that it develops weighting function in C^1 with a minimal amount of additional complexity. The increased support does result in an increase in computational effort that is different from the meshless methods which invest a mount of effort to the research of the influence nodes to construct the shape function.

In Eq.(2), the consistent mass matrix, m_{ij} , is

$$m_{ij} = \sum_p m_p N_i(\mathbf{x}_p) N_j(\mathbf{x}_p). \quad (4)$$

In practice, we generally replace m_{ij} with a lumped, diagonal mass matrix so that Eq. (2) becomes

$$m_i \mathbf{v}_i = \sum_p m_p \mathbf{v}_p N_i(\mathbf{x}_p) \quad (5)$$

where lumped mass is

$$m_i = \sum_p m_p N_i(\mathbf{x}_p) \quad (6)$$

The conversation equation for momentum reads,

$$\rho \frac{d\mathbf{v}}{dt} = \nabla \cdot \sigma + \rho \mathbf{b}, \quad (7)$$

where σ is the stress tensor and \mathbf{b} is the body force. The weak form of Eq.(7) based on the standard procedure used in the FEM [28, 29] can be written

$$\int_{\Omega} \rho \delta \mathbf{v} \cdot \frac{d\mathbf{v}}{dt} d\Omega + \int_{\Gamma_t} \delta \mathbf{v} \cdot (\sigma \cdot \mathbf{n} - \mathbf{t}) d\Gamma + \int_{\Omega} \rho \delta \mathbf{v} \cdot \mathbf{b} d\Omega = 0 \quad (8)$$

where \mathbf{n} and \mathbf{t} is the outward normal unit and traction vectors on the boundary.

Since the continuum bodies is described with the use of a finite set of material particles, the mass density can be written as,

$$\rho(\mathbf{x}) = \sum_{p=1}^{N_p} M_p \delta(\mathbf{x} - \mathbf{x}_p) \quad (9)$$

where δ is the Dirac delta function with dimension of the inverse of volume. The substitution of Eq. (9) into Eq. (8) converts the integral to the sums of quantities evaluated at the material particles, namely,

$$m_i \frac{d\mathbf{v}_i}{dt} = (\mathbf{f}_i)^{\text{int}} + (\mathbf{f}_i)^{\text{ext}} \quad (10)$$

where m_i is the lumped mass and the internal force vector is given by

$$(\mathbf{f}_i)^{\text{int}} = - \sum_p^{N_p} M_p \sigma \cdot (\nabla N_i) / \rho_p \quad (11)$$

and the external force vector reads

$$(\mathbf{f}_i)^{\text{ext}} = \sum_{p=1}^{N_p} N_i \mathbf{b}_p + \mathbf{f}_i^c \quad (12)$$

where the vector \mathbf{f}_i^c is the contact force which is the external nodal force not including the body force and is illustrated in the following section.

A explicit time integrator is used to solve Eq. (10) for the nodal accelerations, with the time step satisfying the stability condition. The critical time step is the ratio of the smallest cell size to the wave speed. After the equations of motion are solved on the cell nodes, the new nodal values of acceleration are used to update the velocity of the material particles. The strain increment for each material particle is determined

Figure 2. (See attached Fig2.jpg)The scheme of contact between body p and body q .

with the use of gradient of the nodal basis function evaluated at the material particle position. The corresponding stress increment can be found from the constitutive model. The internal state variables can also be completely updated. The computational mesh may be discarded, and a new mesh is defined, if desired for the next time step. As a result, an effective computational mesh could be chosen for convenience [31].

2.2. Contact algorithm

The GIMP method provides a natural no-slip contact algorithm based on a common background mesh. But natural contact algorithm has two drawbacks: firstly, the premature contact occurs because the velocities of two bodies are mapped on the same nodes though the distance between the bodies may be still two or even more times of the length of cell, which may cause the numerical noise of stress; Secondly, it is impossible to separate the contacting bodies. Bardenhagen et al have proposed a contact algorithm to simulate the interactions of the grains of granular material [40], in which the contact between bodies is handled when the velocity field of individual particles in contact differs from the single, center-of-mass velocity field in the cell containing contacting particles. A multi-mesh mapping scheme is proposed by Hu and Chen [43]. In the multi-mesh mapping scheme, each material lies in an individual background mesh rather than in the common background one. The meshing process of spur gears is simulated by Hu and Chen with their contact algorithm. To avoid interpenetration and allow separation in the gear meshing process, the normal velocity of any particle at the contact surface is calculated in the common background mesh, while the tangential velocity is found based on the corresponding information in respective individual mesh.

In Bardenhagen's and Chen's contact algorithms the premature contact may still occur. In this paper, the criterion of contact consults the distance of the bodies. In the improved contact algorithm, if the velocities of body p and body q are mapped on the same node i (Seen in Fig.2), the distance between body p and q is calculated. We note the distance between body p and q as \mathfrak{R}_i^{pq} , which can be calculated as:

$$\mathfrak{R}_i^{pq} = \mathbf{n}^{pq} \cdot \mathbf{r}_i^p - \mathbf{n}^{pq} \cdot \mathbf{r}_i^q \quad (13)$$

where \mathbf{n}^{pq} is the normal direction of the contacting interface pointing from body p to q . \mathbf{r}_i^p and \mathbf{r}_i^q are the vectors pointing to node i from body p and body q , respectively. $\mathbf{n}^{pq} \cdot \mathbf{r}_i^p$ and $\mathbf{n}^{pq} \cdot \mathbf{r}_i^q$ can be chosen as

$$\mathbf{n}^{pq} \cdot \mathbf{r}_i^p = \max \{ \mathbf{r}_i^{p^m} \cdot \mathbf{n}^{pq}, m = 1, 2, \dots, N_p \text{ and particle } p^m \in \text{body } p \} \quad (14)$$

$$\mathbf{n}^{pq} \cdot \mathbf{r}_i^q = \min \{ \mathbf{r}_i^{q^m} \cdot \mathbf{n}^{pq}, m = 1, 2, \dots, N_q \text{ and particle } q^m \in \text{body } q \} \quad (15)$$

where $\mathbf{r}_i^{p^m}$ and $\mathbf{r}_i^{q^m}$ are the vectors pointing to node i from particle p^m and q^m , N_p and N_q are the numbers of particles belonging to body p and q , respectively.

The the criterion of contact can be written as

$$\mathfrak{N}_i^{pq} \leq \frac{L}{2}, \quad (16)$$

where L is the length of cell. If Eq.(16) is satisfied, the velocities of p and q are adjusted to new values so that the normal components of them are equal, then the strain and stress of all the particles are updated. So, Eq.(16) plays the role of a switch function. Once bodies p and q contact, they move together along the normal until they separate, so the acceleration along the normal of body p is equal to that of q during the course of the contact. That is

$$\mathbf{a}_i^p \cdot \mathbf{n}_i^{pq} = \mathbf{a}_i^q \cdot \mathbf{n}_i^{pq} \quad (17)$$

where \mathbf{a}_i^p and \mathbf{a}_i^q are the accelerations of bodies p and q at node i , respectively. They can be obtained from the Newtonian second law. Also the normal contact force f_i^{nor} can be derived. Note that the normal contact force must be nonnegative. So, once f_i^{nor} is negative, body p and q is not in contact in the next time step.

If without friction, the contact algorithm has been finished up to now. In the case with friction the Coulomb friction is applied to calculate the tangential contact force.

2.3. Constitutive model and the Equation of State

In this paper, the material is modeled using von Mises plasticity with linear harding [3]. A plastic model dictates a linear elastic response until a yield criterion is reached. The von Mises yield criterion is $3J_2 - Y^2 = 0$, where Y is the plastic yield stress, J_2 is the second invariant of \mathbf{s} , $J_2 = \frac{1}{2}\mathbf{s} : \mathbf{s}$, \mathbf{s} is the deviatoric stress tensor, $\mathbf{s} = \sigma - \text{Tr}[\sigma]/3$. The linear hardening means that Y increases linearly with the second invariant of the plastic strain tensor. If $3J_2 > Y^2$, the increment of equivalent plastic strain $d\varepsilon_p$ can be calculated as $d\varepsilon_p = (\sqrt{3J_2} - Y)/(3G + E_{\text{tan}})$, where G and E_{tan} are the shear and harding modulus, respectively. The increment of the plastic energy can be calculated as $dW_p = d\varepsilon_p \cdot Y$. It is totally translated into the internal energy.

The pressure P is calculated by using the Mie-Grüneissen state of equation which can be written as

$$P - P_H = \frac{\gamma(V)}{V} [E - E_H(V_H)] \quad (18)$$

This description consults the Rankine-Hugoniot curve. In Eq.(18), P_H , V_H and E_H are pressure, specific volume and energy on the Rankine-Hugoniot curve, respectively. The relation between P_H and V_H can be estimated by experiment and can be written as

$$P_H = \begin{cases} \frac{\rho_0 c_0^2 (1 - \frac{V_H}{V_0})}{(\lambda - 1)^2 (\frac{\lambda}{\lambda - 1} \times \frac{V_H}{V_0} - 1)^2}, & V_H \leq V_0 \\ \rho_0^2 c_0^2 (\frac{V_0}{V_H} - 1), & V_H > V_0 \end{cases} \quad (19)$$

where c_0 is the sound speed, λ is the parameter in the linear ration, $U_s = c_0 + \lambda U_p$, U_s and U_p are shock velocity and velocity of particle, respectively. In this paper, the coefficient of Grüneissen $\gamma(V_H)$ is taken as a constant and the transformation of specific

internal energy $E - E_H(V_H)$ is taken as the plastic energy. Both the shock compression and the plastic work cause the increasing of temperature. The increasing of temperature from shock compression can be calculated as:

$$\frac{dT_H}{dV_H} = \frac{c_0^2 \cdot \lambda(V_0 - V_H)^2}{c_v[(\lambda - 1)V_0 - \lambda V_H]^3} - \frac{\gamma(V)}{V_H} T_H. \quad (20)$$

where c_v is the specific heat. Eq.(20) can be resulted with thermal equation and the Mie-Grüneisen state of equation [45]. The increasing of temperature from plastic work can be calculated as:

$$dT_p = \frac{dW_p}{c_v} \quad (21)$$

Both the Eq.(20) and the Eq.(21) can be written as the form of increment. In the present work the thermal dissipation is not taken into account. Such a treatment is reasonable for cases where the propagation speed of shock is much faster than that of the thermal dissipation.

The material constants are chosen to model the energetic crystal high melting explosive. The elastic modulo is 11.87GPa, the poisson ratio is 0.25, the density is $1.9 \times 10^{-3} \text{g/mm}^3$, the initial yield strength is 100MPa, the hardening modulus is 0MPa, the heat capacity is 1250J/(Kg · K). The coefficient of Grüneisen is taken as 1.1, λ is 2.6 and the sound speed c_0 is 2740m/s [1].

3. Results

In this paper we focus on the two-dimensional case. The shock wave to material target is loaded via the impacting by a second material block with symmetric configuration and opposite velocity. The initial shock is along the vertical direction. We apply periodic boundary conditions to simulated system in the horizontal direction. As the first step, we set a single cavity in the HMX block. Such a simulation model corresponds also to a very wide system with a row of cavities being parallel to the impacting plane. We study various cases with different cavity radius and with different strengths of shock. The influence of existing cavity to the contact of bodies is investigated and a secondary impacting is observed. In the cases of strong shock, the influence of cavity size and the impact speed to the “hot-spot” is systematically investigated.

3.1. Validation of the improved contact algorithm

The newly proposed contact algorithm is validated by simulating the impacting of two identical solid bodies having opposite velocities in vertical direction. The initial speed of each body is set to be 300m/s. Initially, the distance between the two bodies is set as 4mm. The width and height of blocks are set to be 40mm and 50mm, respectively. Fig.3 shows the pressure along the vertical direction calculated by different contact algorithms, where the impacting interface is at $y = 0$. From the numerical results we can see that both the GIMP with Bardenhagen’s contact algorithm and the MPM without contact

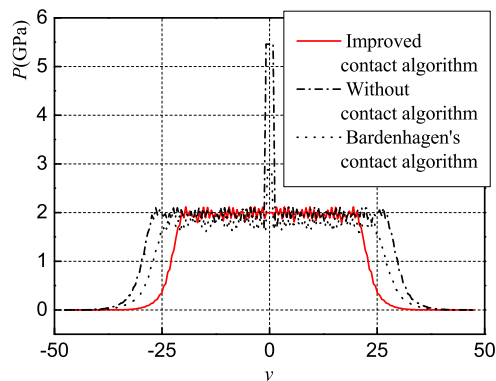


Figure 3. (Color online) Pressure distribution along the vertical direction at time $t = 0.014\text{ms}$. The impacting interface is at $y = 0$. Previous contact algorithms present unreasonable too high pressure in the vicinity of the impact interface.

algorithm give an unreasonable and too high pressure in the vicinity of the interface corresponding to a severe numerical premature contact (See the dash-dotted and dotted lines in the figure). The result by the improved contact algorithm is much better (See the red line in the figure). It is well-known that spurious “wall-heating” phenomenon is generally difficult to eliminate for computational fluid dynamics and computational solid dynamics. Here, our new contact scheme decreases the “wall-heating” phenomenon to an extent that is nearly undistinguishable.

3.2. Dynamical response to weak shock

Due to the ability of withstanding the deformation of shear and tension, cavities in the solid material will not collapse when the shock is very weak. Fig. 4 shows a series of snapshots for a case with an initial impact speed of 150m/s. The size of blocks is the same as section 3.1 and the radius of each cavity is 10 mm. The global procedure can be described as follows:

(a), The two bodies get contact and a shock wave is loaded to each. The shock waves in the two bodies move forwards to the two cavities. The pressure of shock is about 900MPa(See Fig.4(a)).

(b), The shocks arrive at the cavities, then rarefactive waves are reflected back to material in between the two cavities. The cavities begin to shrink in a nearly isotropic fashion(See in Fig4(b)).

(c), The rarefactive waves reach the surface of contacting, then the two bodies begin to separate(See in Fig.4(c)). Note that if there is no cavity inside, the two bodies will not separate so early.

(d), The two bodies continue to separate until the distance between the two bodies reaches the maximal value(See in Fig.4(d)), then the two bodies begin to move closer again because the particles, being above the upper cavity and down the lower cavity, are

Figure 4. (See attached Fig4.jpg) Snapshots for the impact of two blocks with a single cavity in each. Impact velocity of each block is $v = 150\text{m/s}$. From black to white the gray level in the figure shows the increase of local pressure. The unit of pressure is MPa. (a) $t = 0.004\text{ms}$, (b) $t = 0.008\text{ms}$, (c) $t = 0.014\text{ms}$, (d) $t = 0.025\text{ms}$, (e) $t = 0.06\text{ms}$, (f) $t = 0.18\text{ms}$.

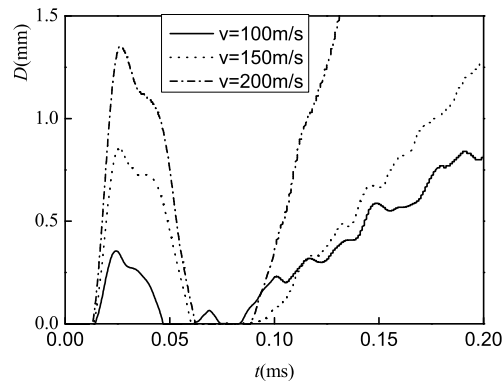


Figure 5. The separation distance versus time t for different impacting speeds shown in the legend. D represents half of the distance between the two impacting surfaces. Before the occurrence of the secondary impact, D has a maximum value D_{\max} which increases with the impacting speed.

still moving towards the contacting surface, which draws the separating bodies back.

(e), The approaching two bodies collide again. They stay together until the rarefactive waves reflected from the lowermost and the uppermost free surfaces arrive at the contacting surface. Then, they will separate again (See in Fig.4(e)).

(f), After e, the two bodies separate. This is the final separation. The terminal configuration of cavities are still approximately circular. From the whole procedure, we can see that, due to the existence of cavities, the two bodies get a secondary impacting.

In order to comprehend more clearly the phenomena of the secondary impacting, we alter the impacting speed (in the limit of no collapse) and the size of cavity. Fig.5 shows the effects of the initial impacting speed to the maximum separation distance between the two bodies after the first impacting. In Fig.5, D represents half of the distance between the two impacting surfaces. It varies with time t . The initial impacting speed is set as 100m/s , 150m/s and 200m/s , respectively. In all cases the phenomena of the secondary impacting are observed. The maximum value of D is denoted by D_{\max} . The larger the initial impacting speed, the larger the value of D_{\max} .

Fig.6 shows the effects of cavity size on the separation distance between the two impacting bodies. Here D and D_{\max} have the same meanings as in Fig.5. The initial radius of each cavity is set as 6mm , 8mm and 10mm , respectively. It can be seen that the larger the radius of cavity, the larger the value of D_{\max} . That is to say, the larger the cavities, the easier to observe the phenomenon of the secondary impacting. Naturally, if the radius of cavity diminishes to zero, the secondary impact disappears.

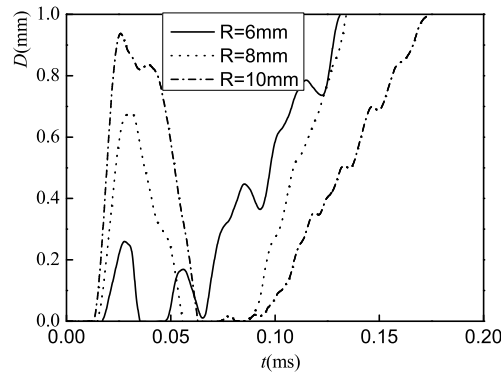


Figure 6. The distance of separation versus time t for different cavity sizes shown in the legend. Here D and D_{\max} have the same meanings as in Fig.5.

Figure 7. (See attached Fig7.jpg) Snapshots for the impacting process of two blocks with a single cavity. The initial radius of cavity 10mm, impact speed $v = 300\text{m/s}$. From blue to red, the local pressure increases. The unit of pressure is Mpa. $t = 0.008\text{ms}$ in (a), $t = 0.012\text{ms}$ in (b), $t = 0.02\text{ms}$ in (c), $t = 0.024\text{ms}$ in (d).

3.3. Dynamical response to strong shock

If the shock is strong, asymmetric collapse of the cavity will occur. When the radius of cavity is set to be 6mm, 8mm and 10mm, respectively, the corresponding minimum impact speed v for the cavity to collapse asymmetrically is 120m/s, 150m/s and 200m/s, respectively. That is to say, the smaller the radius of cavity, the easier for the cavity to collapse asymmetrically. This is because larger curvature is easier to accumulate particles. The course of the collapse of the upper cavity can be described as follows: When the shock reaches the cavity, the upstream side of cavity will reflect a rarefactive wave which propagates downwards. See Fig.7(a). This causes the pressure in the region close to the upstream side of the cavity is lower than around. Then, the neighboring particles accumulate towards to the lower side of cavity, which will accelerate the upward speed of particles there. There are two factors that influence the deformation of the cavity. One is the the accumulation of the particles to the lower side of the cavity, the other is the resistance of the solid material to shear. The competition of the two factors determines how the cavity deforms. Obviously, as the impact speed increases, the resulted shock becomes stronger, then the influence of the accumulation of the particles becomes stronger. If the strength of the material close to the lower side of the cavity cannot withstand the accumulation of particles, the upward speed of particles will become larger and larger, and the cavity will collapse asymmetrically. The upward speed of these particles in Fig.7(a) is about 550m/s, increases to 844m/s in Fig.7(b), reaches 1000m/s and a jet can be observed in Fig.7(c), after that, these particles rush to the upper side of cavity at a speed about 1000m/s. At the time of Fig.7(d) the jet just impacts the upper side of cavity, which causes of a distinct increase of pressure.

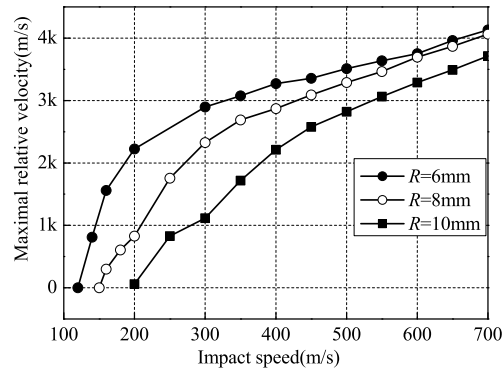


Figure 8. The maximum relative velocity versus the initial impacting speed. The radius of cavity is set as 6mm, 8mm and 10mm, respectively.

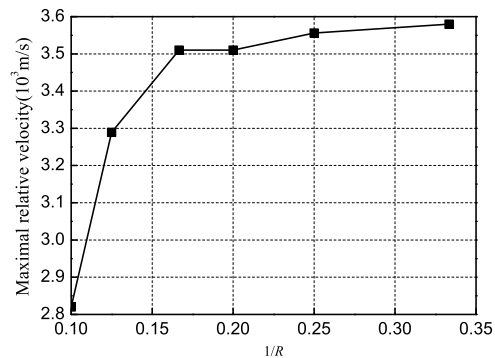


Figure 9. The maximum relative velocity versus the radius of cavity. The impact speed is set as 500m/s.

The course of collapsing of the lower cavity is similar.

To quantitatively describe the collapsing procedure of the shocked cavity, we measure the maximum speed of particles being close to the upper-stream wall relative to that being close to the down-stream wall. Fig.8 shows the maximum relative velocity versus to the impacting speed. For the investigated cases, the former increases nonlinearly with the impacting speed and approaches to a constant; the smaller the initial radius, the larger the maximum relative velocity. A specific case with an impacting speed $v = 500$ m/s is shown in Fig.9. The approached constant is about 3.58Km/s.

Also, the phenomena of the secondary impacting are observed in cases the with strong shock. Fig.10 shows the effects of initial impacting speed v on the separation distance D between the two impacting bodies. The initial impacting speed v is set as 230m/s, 300m/s, 500m/s and 700m/s, respectively. Contrast to the cases with weak shock, D_{\max} doesn't increase monotonously with the initial impact speed.

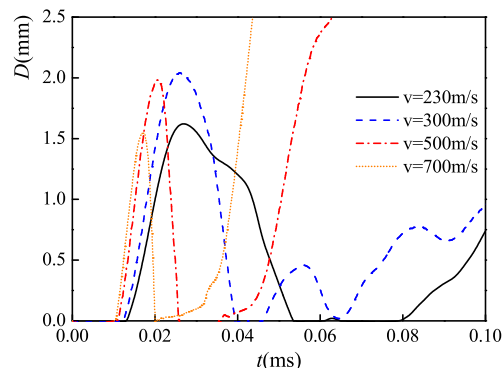


Figure 10. (Color online) The separation distance versus time t for different impacting speeds with strong shock. Here D has the same meaning as Fig.5

Figure 11. (See attached Fig11.jpg) Snapshots for the impact of two blocks with a single cavity in each. Impact velocity $v = 300\text{m/s}$. From blue to red, the color in the figure shows the increase of local temperature. The unit of temperature is K. (a) $t = 0.004\text{ms}$, (b) $t = 0.006\text{ms}$, (c) $t = 0.014\text{ms}$, (d) $t = 0.020\text{ms}$, (e) $t = 0.025\text{ms}$, (f) $t = 0.030\text{ms}$.

When the initial impact speed is not very large (lower than 300m/s), D_{\max} increases correspondingly; but when the impact speed is large (higher than 300m/s), D_{\max} decreases. The critical case with $v = 300\text{ m/s}$ is referred to Fig.7. A physical explanation based on the case with $R = 10\text{ mm}$ is as below. When the impacting speed v is lower than 300 m/s (see Fig. 4), the cavities shrink but without jetting. The strength of the rarefactive wave increases with the initial impacting speed v . When v is larger than 300 m/s , the cavities collapse and cave-in which dissipates a considerable amount of the kinetic energy. The amount of the dissipated energy exceeds the increasing of the total kinetic energy via increasing v . Therefore, the strength of the rarefactive waves do not increase with v but decrease.

3.4. On “hot-spots”

The reactivity of porous energetic material depends greatly on the nature of the “hot-spots” formed by shocks as they move through the material. As observed in the gas-gun experiments [44], coarse HMX produce “hot-spots” that are large enough to persist for a long time whereas fine material seems to produce “hot-spots” that are smaller in size and dissipate quickly. The threshold-to-initiation is the limit where exothermic chemical energy release is balanced by energy dissipated away from the “hot-spot” reaction. In the work of Baer, et al [1], the mesoscale processes of consolidation, deformation and reaction of shocked porous energetic materials are studied using shock physics analysis of impact on a collection of discrete HMX “crystals”. In our work, we focus on the “hot-spots” produced in the shocked HMX material with cavities.

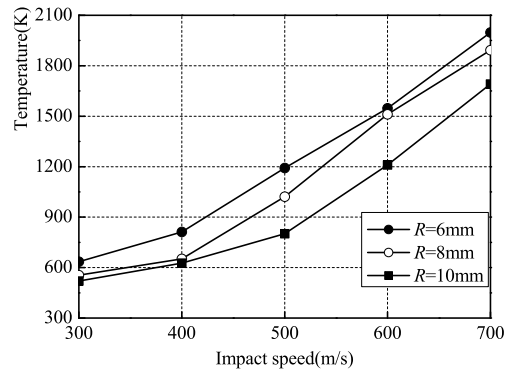


Figure 12. The impact speed dependence of the temperature of the “hot spot”. The radius of cavities is set as 6mm, 8mm and 10mm, respectively. The unit of temperature is K.

Fig.11 shows the global procedure of the production of the “hot-spots”. The impact speed is 300m/s, the initial sizes of blocks are the same as those in section 3.1, and the initial radius of every cavity is 10mm. The initial temperature of the simulated system is 300K. In order to exhibit clearly, only the upper block is shown. The procedure can be described as follows,

(a), The two blocks collide and the shocks begin to propagate towards the cavities. The temperature in the shocked pure HMX is about 310K(See in Fig.11(a)).

(b), The shocks reach the cavities, then rarefactive waves are reflected back from the upstream boundaries of the cavities, the temperatures in the regions which are first shocked and then rarefacted by waves decrease a little (See in Fig.11(b)).

(c), The shocks continue to propagate. The sizes of the cavities reduce as time goes on, the vertical deformation is more serious than the horizontal one. Opposite to the last item, the temperatures in the regions neighboring to the upstream sides of cavities increase. The reason is that the plastic work increases continuously (See in Fig.11(c)).

(d), A jet appears in each cavity, and the temperature of jet material increases as time goes on(See in Fig.11(d)).

(e), The jet material impacts the downstream side of the cavity, which cause a distinct increase of temperature to about 520K (See in Fig.11(e)).

(f), The cavities continues to collapse until they are crammed, a “hot-spot” with the temperature about 520K is produced in each colliding region (See in Fig.11(f)).

Fig.12 shows the temperatures of “hot-spot” produced by different impact speeds for different sizes of cavities. It can be seen that the temperature increases nearly parabolically with the impacting speed v for a fixed size of cavity, which is consistent with the Hugoniot relation, $P = \rho_0(c_0 + \lambda u)$, where $u = v/2$ is the particle speed after shock. At the same time, plastic work increases also nearly parabolically with the impacting speed v . Also, it can be found that the temperature of “hot-spot” produced in smaller cavity is higher than that in larger ones with the same impact speed. As

analyzed in section 3.3, the maximum relative speed produced by smaller cavities is larger than that by larger ones, which cause higher temperature, for the investigated cases.

4. Conclusion

The dynamical response of high melting explosive with cavities under shock is investigated by the generalized interpolation material point method where the criterion for contacting is improved. An elastic-to-plastic and thermal-dynamical model with the Mie-Grüneisen equation of state consulting the Rankine-Hugoniot curve is used to simulate the mechanical and thermal behaviors. A phenomena of secondary impacting is observed for the case of colliding of two bodies with a single cavity in each. For weak shocks, the cavities shrink in a nearly symmetric way, the phenomena of secondary impacting becomes more distinctly as the impact speed increases. But for strong shocks, the situation becomes complex because the asymmetric collapse of cavity influences the reflection of shock. The course for the collapse of cavity is studied for various cavity sizes. For the checked cases, smaller cavities collapse more easily. Our numerical results show that the existence of cavities greatly help the creation of “hot-spots” with a much higher temperature, which is very important for igniting of the explosive materials. The influence of various factors, including impact speed, size of cavity, to the temperature of “hot-spots” is investigated. The temperature of “hot-spots” increases nearly parabolically with the impact speed for a fixed cavity size. The smaller the cavity, the higher the temperature of “hot-spots”, for cases investigated. If the cavity is too small, the effects of cavity collapse becomes very weak. Future work includes the incorporation of thermal diffusion, strain rate effects, etc into the simulations, and cases with cavities filled by gases.

Acknowledgments

We warmly thank Shigang Chen, Haifeng Liu, Song Jiang, Xingping Liu, Xijun Yu, Zhijun Shen, Yangjun Ying, Guoxi Ni, Yun Xu and Yingjun Li for helpful discussions. We acknowledge support by Science Foundation of Laboratory of Computational Physics, National Science Foundation (Grant Nos.10702010 and 10775018) and National Basic Research Program (Grant No. 2002BC412701) of China.

References

- [1] M. R. Baer, M. E. Kipp and F. van Swol, *Micromechanical Modeling of Heterogeneous Energetic Materials*, 1998 The 11th International Detonation Symposium, Snowmass
- [2] N.K.Bourne, 2002 *Shock Waves* **11** 447
- [3] Aiguo Xu, X.F.Pan, Guangcai Zhang, and Jianshi Zhu, 2007 *J. Phys.: Condens. Matter* **19** 326212
- [4] F. P. Bowden, A. D. Yoffe, 1952 *Initiation and growth of explosion in liquids and solids*, Cambridge Univ. Press
- [5] J. Kang, P. B. Butler and M. R. Baer, 1992 *Combrust Flame*. **89** 117

- [6] C. L. Mader, J. D. Kershner, *The Three-dimensional hydrodynamic hot spot model*, 1985 Proc 8th Symp(Int) Detonation, Albuquerque, New Mexico, pp.42-52
- [7] C. L. Mader, J. D. Kershner, *The heterogeneous explosive reaction zone*, 1989 Proc 9th Symp(Int) Detonation, Portland, Oregon, pp.693-700
- [8] C. L. Mader. 1979 *Numerical modelling of detonations*, Univ Calif, Berkeley. Press
- [9] S. R. Cooper, D. J. Benson and V. F. Nesterenko, 2000 International Journal of Plasticity. **16** 525
- [10] N. K. Bourne, *Cavity Collapse in a heterogeneous commercial explosive*, 1989 Proc 9th Symp(Int) Detonation, Office of the chief of Naval Research, Arlington, Virginia, pp.869-878
- [11] N. K. Bourne, J. E. Field, 1999 Proc Roy Soc Lond A. **455** 2421
- [12] Jean-Bernard Maillet, *MD simulations of Hotspots*, 2003 Session K1 - Energetic Materials and Detonation VII
- [13] Brad Lee Holian, Timothy C. Germann, Jean-Bernard Maillet and Carter T. White, 2002 Phys. Rev. Lett. **89** 285501
- [14] Qili Yang, Guangcai Zhang, Aiguo Xu, Yanhong Zhao, Yingjun Li, 2007 Acta Physica Sinica (in Chinese)(in press).
- [15] X Zhang, K Z Song and M W Lu, 2003 Chinese Journal of Computational Mechanics. **14** 91
- [16] Albert Nichols, Craig Tarver and Estella McGuire, *ALE3D Statistical Hot Spot Model Results for LX-17**, 2003 Session K1-Energetic Materials and Detonation VII
- [17] F. H. Harlow, 1964 *Methods for Computational Physics*, Vol. **3**, 319-343, Adler B, Fernbach S, Rotenberg M (eds). Academic Press: New York
- [18] S. G. Bardenhagen and J. U. Brackbill, 1998 J. Appl. Phys. **83**, 5732
- [19] R. A. Gingold, J. J. Monaghan, 1977 Monthly Notices of the Royal Astronomical Society. **181** 375
- [20] J. W. Swegle, D. L. Hicks and S. W. Attaway, 1995 J. Comput. Phys. **116** 123
- [21] P. W. Randles, L. D. Libersky, 1996 Computer Methods in Applied Mechanics and Engineering. **139** 375
- [22] L. D. Libersky, P. W. Randles, R. Vignjevic and N. K. Bourner, *Numerical Simulations of void Collapse Using a Lagrangian Meshfree Particle method*, 2003 Session K1-Energetic Materials and Detonation VII
- [23] K. Tanaka, *Shock Compression of Solid with Voids by Gridless Lagrangian SPH*, 2005 Proceedings of the Conference of the American Physical Society Topical Group on Shock Compression of Condensed Matter.
- [24] Tao Hong, Pei Wang, 2004 Chinese Journal of Energetic Materials. **12** 509 (in Chinese)
- [25] Michael P. Allen, 2004 Computational Soft Matter: From Synthetic Polymers to Proteins. **23** 1
- [26] S. G. Bardenhagen, 2000 Comp. Meth. Eng. Sci. **1**, 11
- [27] D. Burgess, D. Sulsky, J. U. Brackbill, 1992 J. Comput. Phys. **103** 1
- [28] D. Sulsky, Z. Chen, H. L. Schreyer, 1994 Comput. Methods Appl. Mech. Engrg. **118**, 179
- [29] D. Sulsky, J. U. Brackbill, H. L. Schreyer, 1995 Comput. Phys. Comm. **87**, 236
- [30] D. Sulsky, H. L. Schreyer, 1996 Comput. Methods in Appl. Mech. and Eng. **139** 409
- [31] X. F. Pan, Aiguo Xu, Guangcai Zhang, 2007 GF report of China, (No. GF-A0093306G); 2007 Commun. Theor. Phys. (in press); Arxiv.org.0708.3532.
- [32] Z. Wiechowski, 2004 Comput Methods Appl. Mech. Engrg. **193**, 4417
- [33] C. J. Coetzee, P. A. Vermeer and A. H. Basson, 2005 Int. J. Numer. Anal. Meth. Geomech. **29**, 879
- [34] Honglai Tan, John A. Nairn, 2002 Comput. Methods Appl. Mech. Engrg. **191**, 2095
- [35] Joris J. C. Remmers, René, Alan Needleman, 2005 VIII International Conference on Computational Plasticity, Barcelona
- [36] Z. Chen, W. Hu. L. Shen, X. Xin, R. Brannon, 2002 Engineering Fracture Mechanics. **69**, 1873
- [37] Z. Chen, R. Feng. X. Xin and L. Shen, 2003 Int. J. Numer. Meth. Engrg. **56**, 1979
- [38] X. Zhang, K. Y. Sze, S. Ma, 2006 Int. J. Numer. Meth. Engrg. **66**, 689
- [39] R. Allen, York II, D. Sulsky and Howard L. Schreyer, 1999 Int. J. Numer. Meth. Engrg. **44**, 1429

- [40] S. G. Bardenhagen, J. U. Brackbill, D. Sulsky, 2000 *Comput Methods Appl. Mech. Engrg.* **187**, 529
- [41] S. G. Bardenhagen and J. U. Brackbill, 2000 *Phys. Rev. E* **62**, 3882
- [42] S. J. Cummins and J. U. Brackbill, 2002 *J. Comput. Phys.* **180**, 506
- [43] W. Hu, Z. Chen, 2003 *Computers and structures* **81**, 1991
- [44] S. A. Sheffield, R. L. Gustavsen and M. U. Anderson, “Shock loading of Porous High Explosives”, 1996 *High Pressure Shock Compression of solids, IV, Response of Highly Porous Solids to Shock Loading*, Chap. 2, Springer-Verlag.
- [45] B. Zhang, et al. 1997 *Explosion physics*, Ordance Industry Press, China.

This figure "Fig4.jpg" is available in "jpg" format from:

<http://arxiv.org/ps/0710.2181v1>

This figure "Fig7.jpg" is available in "jpg" format from:

<http://arxiv.org/ps/0710.2181v1>

This figure "Fig11.jpg" is available in "jpg" format from:

<http://arxiv.org/ps/0710.2181v1>